PHYSICAL REVIEW B **109**, 014419 (2024)

Influence of Dy^{3+} environment on magnetic anisotropy and magnetocaloric effect in $Dy_3B_2C_3O_{12}$ (B = In, Sc, Te; C = Ga, Al, Li) garnets

F. Damay,[1,*] S. Petit,[1] D. Sheptyakov,[2] C. V. Colin,[3] E. Suard,[4] S. Rols,[4] J. Embs,[2] U. Stuhr,[2]
D. Bounoua,[1] O. Demortier,[1] and C. Decorse[5]
[1]*Université Paris-Saclay, Laboratoire Léon Brillouin, CEA-CNRS UMR12, F-91191 Gif-sur-Yvette Cedex, France*
[2]*Laboratory for Neutron Scattering and Imaging, Paul Scherrer Institut, CH-5232 Villigen, Switzerland*
[3]*Institut Néel, Université Grenoble-Alpes, CNRS, F-38042 Grenoble, France*
[4]*Institut Laue-Langevin, 71 Avenue des Martyrs, F-38042 Grenoble, France*
[5]*Université Paris-Saclay, Institut de Chimie Moléculaire et des Matériaux d'Orsay, UMR CNRS 8182, F-91405 Orsay, France*

(Received 9 May 2023; accepted 5 December 2023; published 23 January 2024)

In the framework of the general phase diagram published recently for a pseudospin $S = 1/2$ on a hyperkagome network [Kibalin *et al.*, Phys. Rev. Res. **2**, 033509 (2020)], four $Dy_3B_2C_3O_{12}$ garnets with different species on the B and C sites, namely, $Dy_3Sc_2Al_3O_{12}$ (DyScAl), $Dy_3Te_2Li_3O_{12}$ (DyTeLi), $Dy_3Sc_2Ga_3O_{12}$ (DyScGa), and $Dy_3In_2Ga_3O_{12}$ (DyInGa), have been studied by neutron powder diffraction and inelastic neutron scattering, to investigate the impact of B and C substitutions on the Dy^{3+} dodecahedral oxygen environment and crystal field, and thus on the Dy^{3+} spin magnetic anisotropy. In the four compounds, the magnetic ground state is a multiaxis antiferromagnetic order similar to that of $Dy_3Al_5O_{12}$, characterized by an ordered moment close to the theoretical maximum, $\sim 6\ \mu_B$. The gap between the ground state and the first excited crystal electric field level varies from $\sim$3.2 meV (DyInGa) up to 11.2 meV (DyScAl), confirming the rather strong Ising character of the Dy^{3+} moment in those garnets. For a better understanding of the impact of the distortion of the oxygen environment on the Dy^{3+} magnetic anisotropy, point-charge calculations were then performed, mapping a magnetic anisotropy diagram versus a wide range of distortions. Results show that Ising-like behaviors mostly predominate, associated with large g_x, g_y, or g_z Landé values, whose stable area is determined by the shape of the DyO_8 cage. Magnetic entropy calculations confirm that the magnetocaloric effect increases sharply near those boundaries and validate the use of dysprosium garnets for low temperature, low magnetic field adiabatic demagnetization refrigeration cryostats.

DOI: 10.1103/PhysRevB.109.014419

I. INTRODUCTION

In recent years, magnetic refrigeration, a method used to cool matter through magnetic field cycling via the magnetocaloric effect (MCE), has been extensively studied as an alternative technique to conventional gas compression [1–4]. The magnetocaloric effect corresponds to the isothermal magnetic entropy change ($-\Delta_{SM}$), or to the adiabatic temperature change, of a solid exposed to a changing magnetic field. For low temperature (below 10 K) magnetocaloric cooling, a variety of materials have been investigated, such as paramagnetic salts [5], intermetallic alloys [6], or frustrated magnets such as pyrochlores [7]. Rare-earth garnets $R_3B_2C_3O_{12}$ have also a high potential for adiabatic demagnetization refrigeration applications, as exemplified by studies on $R_3Ga_5O_{12}$ (R = Tb, Gd, Dy) [8], or $Yb_3Ga_5O_{12}$ [9]. The use of rare earths with large magnetic moments J is always favored indeed, since in theory the maximum entropy change that can be reached is $-\Delta_{SM} = R\ln(2J+1)$. In real materials, however, the presence of a crystal electric field (CEF) around the rare earth leaves only one (or more) doublets free at low temperature. This CEF scheme decreases the maximum entropy change that can be reached, provided in addition that one keeps away from any magnetic ordering transition, which, in the case of most rare-earth garnets, takes place, conveniently, below $T_N \approx 2$ K.

Crystal electric field schemes vary depending on the nature of the rare earth, a consequence of which can be seen, for instance, in the variety of magnetic anisotropies (another macroscopic manifestation of the CEF) displayed by rare-earth gallium garnets, from the isotropic ("Heisenberg") case [10–15] (R = Gd, Yb), to the Ising case, as in $Tb_3Ga_5O_{12}$ [16–18] or $Er_3Ga_5O_{12}$ [19]. In addition, for a given rare earth, it is also very sensitive to the environment of the latter: it was shown lately in R = Dy garnets that the rare-earth CEF scheme is influenced by the cations on the B and C sites, going from a strong Ising behavior in $Dy_3Al_5O_{12}$ (DyAl) to a planar one in $Dy_3Ga_5O_{12}$ (DyGa) [20].

It is therefore crucial to get a better understanding of how the environment around the rare earth impacts its CEF scheme, and how this in turn affects magnetocaloric properties. Such a relationship between $-\Delta_{SM}$ and crystal-field effects has been tackled very recently in HoB_2 [21], but has never been studied systematically within a structural type thus far.

We address this issue in this paper by comparing four garnets, with different ions on the B and C sites: $Dy_3Sc_2Al_3O_{12}$, $Dy_3Te_2Li_3O_{12}$, $Dy_3Sc_2Ga_3O_{12}$, and $Dy_3In_2Ga_3O_{12}$. Detailed structural information was obtained systematically using

---

[*] Corresponding author: francoise.damay@cea.fr

neutron powder diffraction, and completed by inelastic neutron scattering experiments to characterize the low energy CEFs. Point charge followed by CEF scheme calculations varying the oxygen positions around Dy were then performed to relate the distortion of the Dy oxygen cage with magnetic anisotropy. Calculations converge towards a picture in which the DyO_8 dodecahedral cage distortion leads to three Ising-like anisotropies, characterized by different easy axes; experimental observations in the Dy garnets studied in this work are described satisfactorily in this picture. Those calculations were also used to evaluate theoretically the variation of magnetic entropy of a single Dy^{3+} ion versus temperature and magnetic field, depending on the Dy^{3+} environment. It shows a significant increase of the magnetocaloric effect at low temperature and low magnetic field for specific cage distortions where magnetic anisotropy nears a boundary between easy axes. Going beyond dysprosium garnets, this approach opens a powerful way to better design rare-earth magnetocaloric compounds, based on the precise control of any rare-earth environment.

II. EXPERIMENT

Powder samples of $Dy_3Sc_2Al_3O_{12}$ (DyScAl), $Dy_3In_2Ga_3O_{12}$ (DyInGa), and $Dy_3Sc_2Ga_3O_{12}$ (DyScGa) were prepared by solid state synthesis, mixing stoichiometric amounts of Dy_2O_3 with appropriate precursors, namely, Ga_2O_3, Al_2O_3, Sc_2O_3, and In_2O_3. Several thermal treatments of at least 48 h were performed in air, in the temperature range $1200 - 1500^\circ$ C with intermediate grindings.

$Dy_3Te_2Li_3O_{12}$ (DyTeLi) was prepared by the same solid state route, from Dy_2O_3, TeO_2, and Li_2CO_3. Since the fusion temperatures of TeO_2 and Li_2CO_3 are very low (slightly higher than 700° C), synthesis was started at 550° C, and the temperature was gradually increased at each thermal treatment, up to a maximum of 750° C. X-ray diffraction was used to follow the progress of all the synthesis reactions.

Neutron powder diffraction (NPD) experiments were carried out on D2B ($\lambda = 1.59$ Å) at Institut Laue-Langevin (ILL, Grenoble, France) at RT [22], and on HRPT ($\lambda = 1.49$ Å and $\lambda = 2.45$ Å) at the SINQ facility of the Paul Scherrer Institute (PSI, Villigen, Switzerland) between 1.5 and 300 K. To minimize neutron absorption, double wall cylinders made with Al foil or Cu foil were used inside the vanadium sample holders. Additional experiments at dilution fridge temperatures were carried out on D1B ($\lambda = 2.528$ Å) for DyScGa and DyInGa [23]. Samples were wrapped in Cu foil before being introduced in a copper sample holder. Rietveld refinements were performed with the FULLPROF program [24]. Symmetry analysis was carried out using the FULLPROF SUITE software and the Bilbao Crystallographic Server [25,26].

Inelastic neutron scattering experiments were carried out on the time-of-flight spectrometer Panther (ILL) for DyScGa and DyInGa at ILL, between 2 and 250 K, varying the incident energy from $E_\mathrm{i} = 10$ meV to 50 meV [27]. DyScAl and DyTeLi were studied on the triple-axis spectrometer Eiger (PSI), with $k_f = 2.662$ Å^{-1}, using a pyrolytic graphite filter on k_f, at 1.5 and 160 K. Additional measurements on DyTeLi were performed on the time-of-flight spectrometer Focus [28], with $\lambda = 2.0$ Å, at 1.5 and 100 K. This experimental setup provided an energy resolution of 1.5 meV.

III. RESULTS

A. Crystal structure of Dy garnets at RT and 5 K

All four $Dy_3B_2C_3O_{12}$ garnets, $Dy_3Sc_2Al_3O_{12}$, $Dy_3Te_2Li_3O_{12}$, $Dy_3Sc_2Ga_3O_{12}$, and $Dy_3In_2Ga_3O_{12}$, synthesized in this work crystallize at RT in the same cubic structure, with space group *Ia*-3*d* [Fig. 1(a)].

The Dy site is the dodecahedral 24*c* (0,0.25,0.125) site, while the *B* and *C* sites correspond to the octahedral 16*a* (0,0,0) and tetrahedral 24*d* (0,0.25,0.375) sites, respectively [Fig. 1(b)]. O^{2-} occupies the 96*h* (*x*, *y*, *z*) site. All sites are fully occupied. Each dodecahedron shares edges with two tetrahedra, four octahedra, and four other dodecahedra [Fig. 1(b)].

Within the resolution of the neutron diffraction experiments, the crystal structure remains cubic *Ia*-3*d* down to 1.5 K. Results of the Rietveld refinements performed on the 5 K high-resolution neutron powder diffraction data of the different Dy garnet samples are summarized in Tables I and II, and illustrated in Fig. 2 in the case of DyTeLi. They are in good general agreement with the structural parameters obtained in [29]. These results show that there is no substitutional disorder on either the rare-earth or the *C* sites. In the specific case of DyTeLi, refinements confirm that Li^+ is in the tetrahedral site [30,31], as expected [29]. On the other hand, in DyScGa, DyInGa, and DyScAl, partial substitution of the *C* site cation (Ga or Al), up to $C_\mathrm{B} = 14\%$, is found on the *B* site. Partial substitution of Dy^{3+} on the *B* site is not observed, however, within the experimental resolution.

As noted in [29], the lattice volume does not vary linearly with the weighed ionic radii of *B* and *C* ($\langle r\rangle = (2r_B + 3r_C)/5$) [32], even corrected by C_B: for DyTeLi, the cubic cell parameter [$a = 12.2982(6)$ Å at 5 K] is much smaller than expected from the calculated $\langle r\rangle$ value, close to that of DyScGa (Table I), suggesting that other effects, such as size mismatch and charge or electronic configuration are at play. The cubic lattice parameter *a* (or the Dy-Dy distance) will thus be used as the comparing variable.

Because the shape of the oxygen dodecahedral cage around the Dy^{3+} cation will impact magnetic anisotropy, it needs to be described carefully [20]. The dodecahedral environment of Dy consists in a low symmetry (D_2) cage involving eight neighboring oxygens, and two sets of Dy-O (×4) distances [Fig. 1(b) and Table II]. Figure 3 illustrates the variation with *a* of the Dy-O distances across the series. It shows that the largest Dy-O (Dy-O2) distance remains fairly constant throughout the studied compounds, around ∼2.46 Å, while the shortest Dy-O (Dy-O1) bond has a linear dependence with *a*, in the interval spanned in this work. The corresponding variance (with respect to a mean Dy-O), shown in the inset of Fig. 3, points out accordingly a regularization of the cage as *a* increases (see, for instance, DyScGa and DyInGa), as the difference between Dy-O bond lengths decreases. This effect is rather subtle, however, with σ evolving only from 1.60(5) (DyInGa) to 2.60(5) (DyTeLi). Table II also gives the various O-O distances within a DyO_8 cage [see Fig. 1(c)], namely,

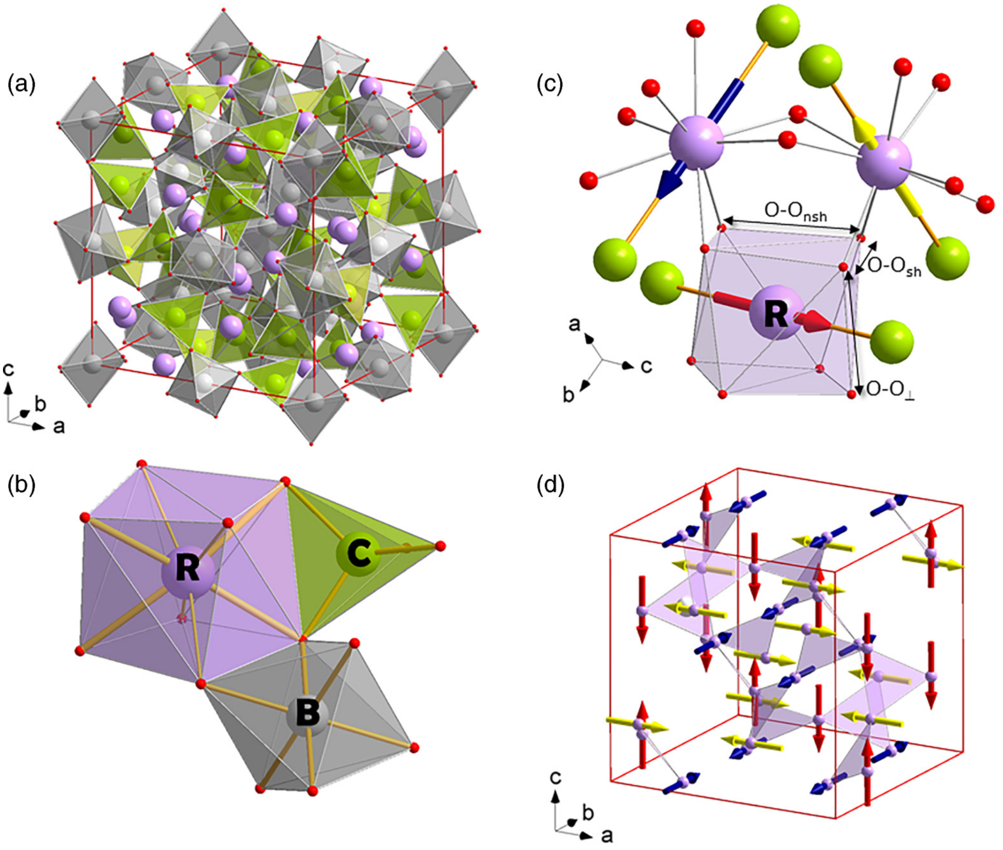

FIG. 1. (a) $R_3B_2C_3O_{12}$ garnet cubic crystal structure [R (rare earth), B and C cations are in purple, gray, and green, respectively, and oxygen anions are in red]. (b) Details of the R (dodecahedral), B (octahedral), and C (tetrahedral) sites. On the R site, the thick and thin bonds indicate the short and long R-O bonds, respectively. (c) Details of the moment anisotropy axis in the Z-Ising case ($g_z \gg g_x,\ g_y$), which is aligned along the direction of the shortest bond between an R and a C site. (d) Antiferromagnetic multiaxis "AFA" magnetic order encountered in Ising rare-earth garnets. Yellow, blue, or red spins on the R sites are parallel to a, b, or c, respectively; the purple triangles identify the two twisted hyperkagome lattices, or three-dimensionnal array of corner-sharing triangles, formed by the R sites in the garnet structure.

O-O$_{sh}$ (shared edge with another dodecahedron), O-O$_{nsh}$, and O-O$_{\perp}$, shortest O-O bond in the third direction. From Table II, it can be observed that O-O$_{sh}$ decreases regularly with increasing r_B, while O-O$_{\perp}$ increases almost linearly with increasing r_C. The ratio O-O$_{sh}$/O-O$_{\perp}$ is <1 for the garnets with Ga^{3+} on the C site.

Another insightful observation is that a more regular DyO$_8$ environment, that is, all Dy-O being equal, can be analytically written as a condition on the oxygen position $y_O = (x_O + z_O)/2$. Because the degree of distortion of the cage is

TABLE I. Crystal structure parameters of various Dy garnets at 5 K, determined from Rietveld refinements of NPD data (HRPT, λ= 1.49 Å). The cell space group is *Ia*-3*d* (# 230). Determination of the ordered magnetic moment was performed fixing the 5 K crystal structure parameters in the magnetic space group *Ia*-3*d'* (#230.148). Ionic radii from [32].

	DyTeLi	DyScAl	DyScGa	DyInGa
r_B (Å)	0.56	0.745	0.745	0.80
r_C (Å)	0.59	0.39	0.47	0.47
$\langle r \rangle$ (Å)	0.58	0.53	0.58	0.60
a (Å)	12.2982(6)	12.3570(6)	12.5047(5)	12.5944(6)
x_O	−0.0261(3)	−0.0314(3)	−0.0284(3)	−0.0282(3)
y_O	0.0515(4)	0.0559(4)	0.0580(4)	0.0597(4)
z_O	0.1453(4)	0.1566(3)	0.1547(4)	0.1570(4)
C_B (%)		14.0	20.1	14.7
R_{Bragg} (%)	2.09	2.35	2.15	2.72
χ^2	1.28	1.27	1.47	1.20
M_T (μ_B)	$6.5(1)_{1.5\,K}$	$7.5(1)_{1.5\,K}$	$6.1(1)_{50\,mK}$	$5.9(1)_{50\,mK}$

TABLE II. Selected distances (Å) at 5 K in Dy garnets. See Fig. 1(d) for the meaning of O-O$_{sh}$ (shared edge), O-O$_{nsh}$ (nonshared edge), and O-O$_{\perp}$ (perpendicular edge).

	DyTeLi	DyScAl	DyScGa	DyInGa
Dy-Dy	3.7655(1)	3.7836(1)	3.8288(1)	3.8562(1)
Dy-O1 (×4)	2.348(2)	2.355(2)	2.372(2)	2.380(2)
Dy-O2 (×4)	2.474(2)	2.461(2)	2.455(2)	2.456(2)
$\langle$Dy−O$\rangle$	2.411(2)	2.408(2)	2.414(2)	2.418(2)
O-O$_{sh}$	2.905(2)	2.769(2)	2.756(2)	2.715(3)
O-O$_{nsh}$	2.586(2)	2.849(2)	2.805(2)	2.858(2)
O-O$_{\perp}$	2.870(2)	2.690(2)	2.790(3)	2.785(3)
B-O (×6)	1.923(2)	2.092(2)	2.096(2)	2.145(2)
C-O (×4)	1.881(2)	1.773(2)	1.846(2)	1.850(2)

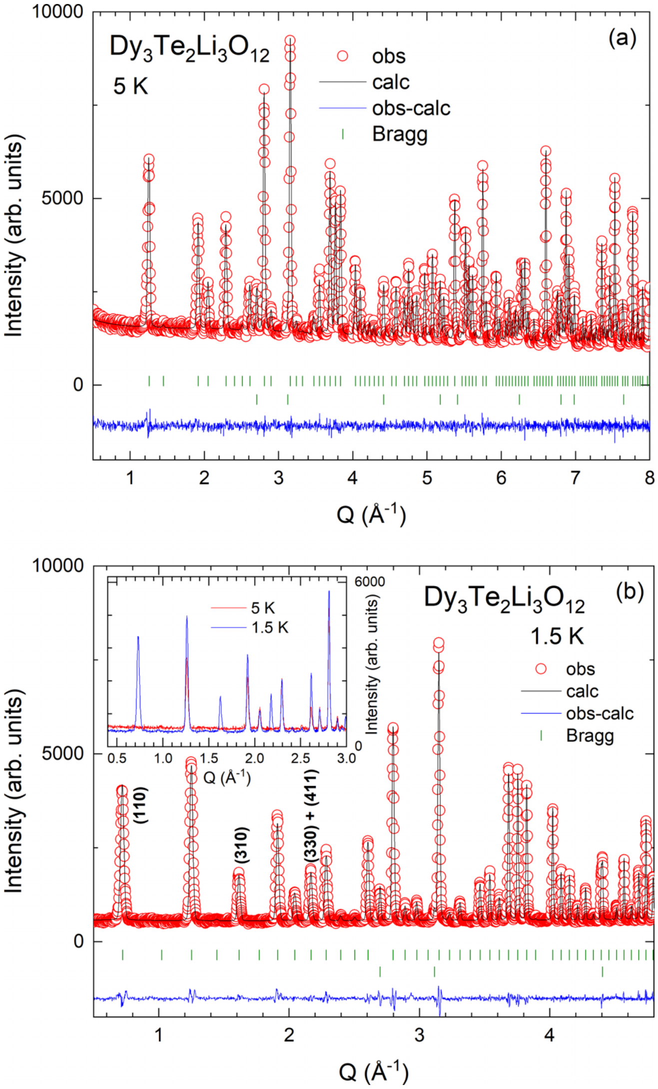

FIG. 2. Rietveld refinement of the 5 K [λ= 1.49 Å, (a)] and 1.5 K [λ= 2.45 Å, (b)] neutron powder diffractograms of $Dy_3Te_2Li_3O_{12}$. (Experimental data, red dots; calculated profile, black continuous line; allowed Bragg reflections, green vertical marks. The difference between the experimental and calculated profiles is displayed at the bottom of the graph as a blue continuous line.) The main magnetic peaks are labeled in (b). Inset: NPD data at 5 K and 1.5 K of $Dy_3Te_2Li_3O_{12}$ (λ= 2.45 Å).

difficult to visualize, this relationship will be useful when discussing the point-charge calculations presented later. It also corresponds to a cage built on two parallel oxygen rectangles, that is, to an angle $\varphi = 0$ in the polar description used sometimes in garnets [33].

B. Magnetic order in Dy garnets

Earlier work on rare-earth garnets [29] pointed out an antiferromagnetic behavior for all the Dy compounds studied here, with an antiferromagnetic transition observed on susceptibility $\chi(T)$ curves in 0.01 T at $T_N = 1.97$, 2.17, 1.11, and 1.11 K for DyTeLi, DyScAl, DyScGa, and DyInGa, respectively. To investigate the corresponding magnetic ground states, neutron powder diffraction experiments were systematically carried out below T_N: results indicate that all the garnets of this study order in the so called “AFA” structure [34]. The latter can be described as three sublattices of antiferromagnetic spins parallel to the cubic crystal axis [see Fig. 1(d)], so that on each triangle of the two intertwined Dy^{3+} hyperkagome lattices, the three spins are perpendicular to each other. Rietveld refinements were carried out in the corresponding magnetic space group, *Ia*-3*d’* (#230.148). An example in the case of DyTeLi at 1.5 K is illustrated in Fig. 2(b); the refinement results of all Dy compounds are summarized in Table I. There is a slight variation of the ordered magnetic moment within the series, from a maximum of 7.5 μ_B (DyScAl) to a minimum of 5.9 μ_B (DyInGa), mirroring the decrease of T_N values with the increasing Dy-Dy distance (Fig. 4).

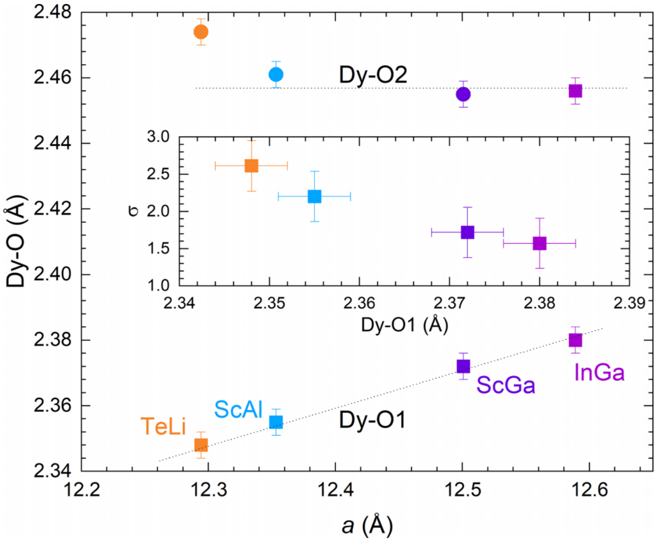

FIG. 3. Evolution with the cell parameter *a* of the Dy-O distances (labeled Dy-O1 and DyO2; see Table II) within the Dy dodecahedral cages for the different Dy garnets studied (at 5 K), and (inset) corresponding evolution with Dy-O1 of the variance σ, defined as $\sigma = 10^2\sqrt{\frac{1}{N}\sum_{i=1}^{N}\left(\frac{\langle d_i-\langle d\rangle\rangle}{\langle d\rangle}\right)^2}$, with *d* defining the Dy-O distances in the cage, and $\langle d\rangle$ their average.

C. Magnetic anisotropy of Dy^{3+} in Dy garnets

Inelastic neutron scattering experiments (Fig. 5) were carried out to study Dy^{3+} crystal electric field excitations in the four garnets studied, to get a correct picture of their magnetic anisotropy. It is already known from the study of DyGa and DyAl [20] that the Dy^{3+} CEF ground state is a doublet, which defines an effective spin-1/2 degree of freedom.

The inelastic excitation spectra of both compounds at 5 K is characterized by a set of nondispersive excitations, whose intensities decrease as the momentum transfer *Q* increases, as expected for CEF excitations. In DyAl, the first and also the most intense excited level is observed at 8.7 meV, while in DyGa, it is seen at much lower energy, around 2.6 meV [Fig. 5(c), from a previous study [20]]. Other crystal-field transitions of lesser intensities are also present in both compounds around 9 and 14 meV, as well as a broad one in the 20–23 meV range [20].

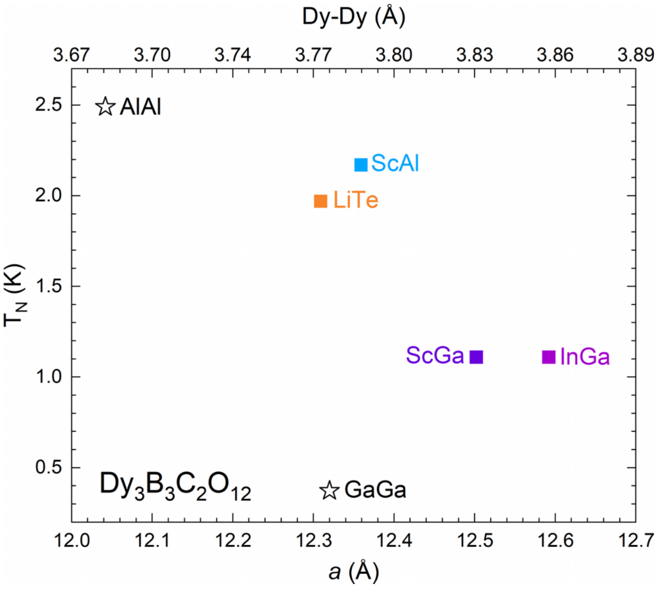

FIG. 4. Evolution with the cell parameter a of the antiferromagnetic ordering temperature T_N for different Dy$_3B_2C_3$O$_{12}$ garnets (from [29] and [20]; labels show the atomic species on the B and C sites).

The excitation spectra of DyTeLi, DyScAl, DyScGa, and DyInGa garnets show a similar behavior at 5 K to that of DyAl or DyGa, with predominant nondispersive excitations attributed to Dy^{3+} crystal-field excitations. A typical $S(Q,E)$ spectrum and its temperature evolution are illustrated in Figs. 5(a) and 5(b) in the case of DyInGa. Both the Q dependence of the nondispersive signal and its temperature evolution confirm the CEF nature of the excitations.

The gap between the first excited CEF level and the ground state being related to the Ising character of the moment (the larger the gap, the stronger the Ising spin character), the comparison of constant $Q = 2.5$ Å^{-1} energy scans at low temperature for DyScAl, DyTeLi, DyScGa, and DyInGa is shown in Fig. 5(c), along with DyGa and DyAl from [20]. The energy of the first excited CEF level ranges from a minimum value of $\sim$2.6 meV in DyGa, to a maximum of $\sim$11.6 meV in DyScAl. Although it is clear that there is no direct relationship between the cell volume and the energy of the first CEF level, one trend emerges nevertheless: the first CEF level is at much lower energy (below 4 meV) in garnets with Ga on the C site, which also happen to be the ones with the largest a parameter and more regular oxygen environment (inset of Fig. 3). A large cation on the C site is not a sufficient condition to achieve this either, as exemplified by DyTeLi with a large Li$^+$ on the C site ($r_{\mathrm{Li}+} = 0.59$ Å $r_{\mathrm{Ga}3+} = 0.47$ Å).

On the other side of the spectrum, DyScAl and DyTeLi, which have the largest dodecahedral distortion, also exhibit the strongest Ising character, with, respectively, first CEF excitations around 11.6 and 6.4 meV. The comparison of DyAl and DyScAl suggests that increasing the size of the B site or the size mismatch between the B and C sites enhances the Ising character, but only a comparison with other compositions, such as Dy$_3$In$_2$Al$_3$O$_{12}$, could confirm this hypothesis.

In addition to its energy, another feature of the CEF excitation is its energy width. As is clear from Fig. 5(c), this width is fairly variable throughout the series: DyTeLi and DyGa have the sharpest low level CEF excitations, while it is much broader in DyScAl, and to a lesser extent, in DyScGa and DyInGa. In the latter two, higher-resolution experiments have actually identified the presence of two levels, at 3.3 and 4.1 meV in DyScGa and 3.2 and 4.3 meV in DyInGa [bottom panel of Fig. 5(c)]. This could reflect the slight compositional disorder evidenced on the B site by neutron diffraction, an effect that has been observed and interpreted as such in other compounds, in particular in several pyrochlores such as R_2GaSbO$_7$ (R = Nd, Yb) [35,36], Nd$_2$ScNbO$_7$ [37,38], or Tb$_2$Sn$_{2-x}$Ti$_x$O$_7$ [39].

D. Point-charge calculations

Crystal electric field energy levels can be calculated on the basis of a point-charge model, as developed in [40]: the electrostatic potential is the sum of the Coulomb potentials created by surrounding ligand atoms, parametrized by their charges and positions. As the aim of the calculations is qualitative rather than quantitative, more complex effects such as shielding parameters [41,42], electronegativity [43], or dipolar/quadrupolar potential corrections [44] were not implemented. The goal is to be able to relate the distortion of the cage (varying the oxygen coordinates x_{O}, y_{O}, and keeping z_{O} = cste) with variations of the Wybourne coefficients involved in the crystal-field Hamiltonian $\mathcal{H}_{\mathrm{CEF}}$ (see Appendix), from which magnetic anisotropy and magnetic entropy are then inferred. It is important to mention here that variations in (x_{O}, y_{O}) are deliberately large, to get an overall picture of the cage distortion impact, but in some areas they do not reflect physically meaningful environments around the Dy^{3+}, particularly regarding Dy-O distances.

We first focus on the evolution with its environment of the calculated magnetic anisotropy of Dy^{3+}. The three Landé factors g_X, g_Y, and g_Z are inferred from the calculation of the magnetic moment matrix projected onto the subspace spanned by the ground state doublet. They are computed as a function of x_{O} and y_{O} oxygen coordinates, and drawn independently for clarity in Fig. 6. Note that, as in [20], for a Dy^{3+} whose anisotropy axis is parallel to [001] (local Z axis) in the structure, local X and Y axes are parallel to [110] and [1 −1 0], respectively. Three regions are noticeably identified, corresponding essentially to predominant X ($g_X \gg g_Y$, g_Z), Y ($g_Y \gg g_X$, g_Z), or Z ($g_Z \gg g_X$, g_Y) Ising anisotropies. Rather sharp boundaries exist over limited distortion ranges, in which intermediate planar anisotropies can be expected, of the XY, XZ, or YZ types. Intersections of those boundaries lead to two isotropic (XYZ) points in the (x_{O}, y_{O}) range investigated. Interestingly, the YZ anisotropy boundary actually corresponds to more regular DyO$_8$ cages, in which all Dy-O are equal [analytically written as $y_{\mathrm{O}} = (x_{\mathrm{O}} + z_{\mathrm{O}})/2$, drawn as a yellow line in Fig. 6]. The environment imposed by the garnet crystal chemistry places DyTeLi, DyScGa, DyScAl, and DyInGa (pink squares in Fig. 6) close to the convergence between the X-, Y-, and Z-Ising phases, that is close to an isotropic case, but still in the Ising Z zone, in agreement with our observations. More anecdotally, there is another isotropic point,

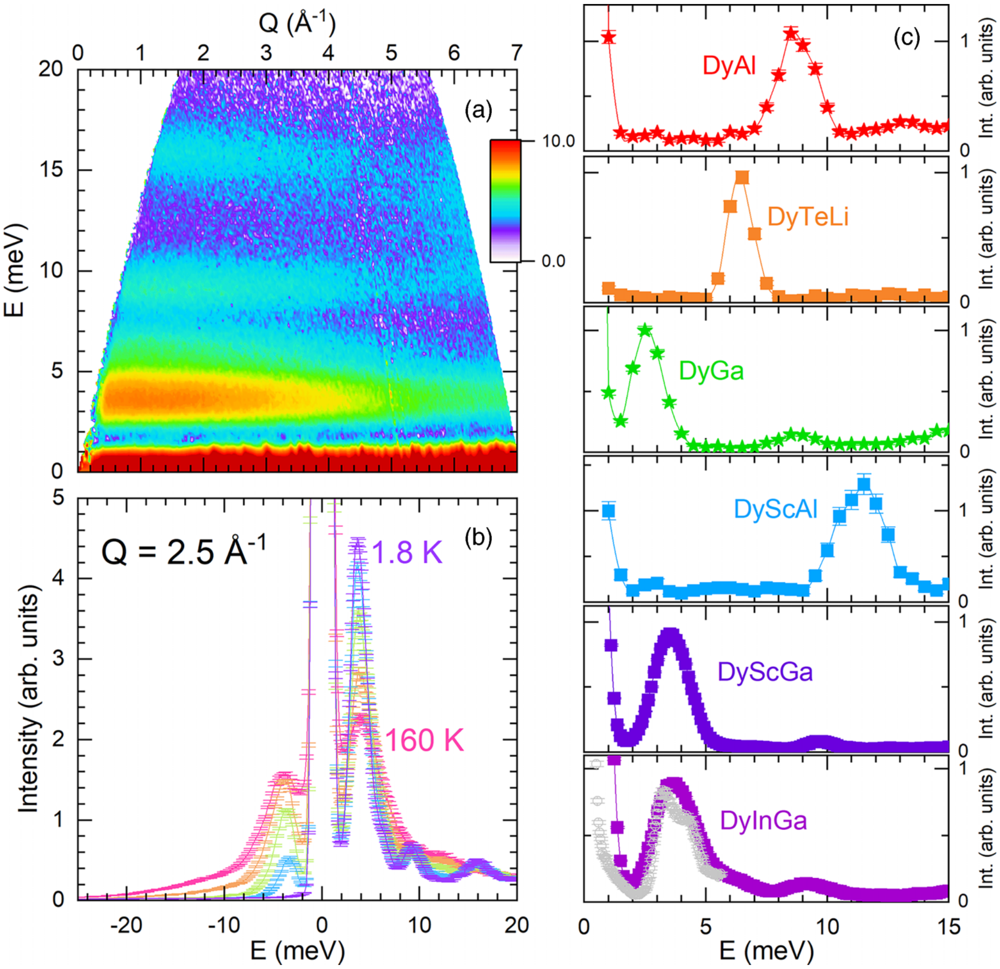

FIG. 5. (a) 1.8 K mapping of the excitation spectrum of DyInGa ($E_i = 30$ meV). (b) Temperature evolution (1.8–160 K) of energy scans at constant $Q = 2.5$ Å^{-1} for DyInGa ($E_i = 30$ meV). (c) Energy scans at constant $Q = 2.5$ Å^{-1} and 5 K for the four garnets of this work, with additional DyAl (red stars) and DyGa (green stars) for comparison. From top to bottom the cell parameter *a* increases. See Experiment section for details on which instrument was used. For DyInGa, a scan at higher resolution ($E_i = 10$ meV) is superimposed in gray to emphasize the existence of two energy levels.

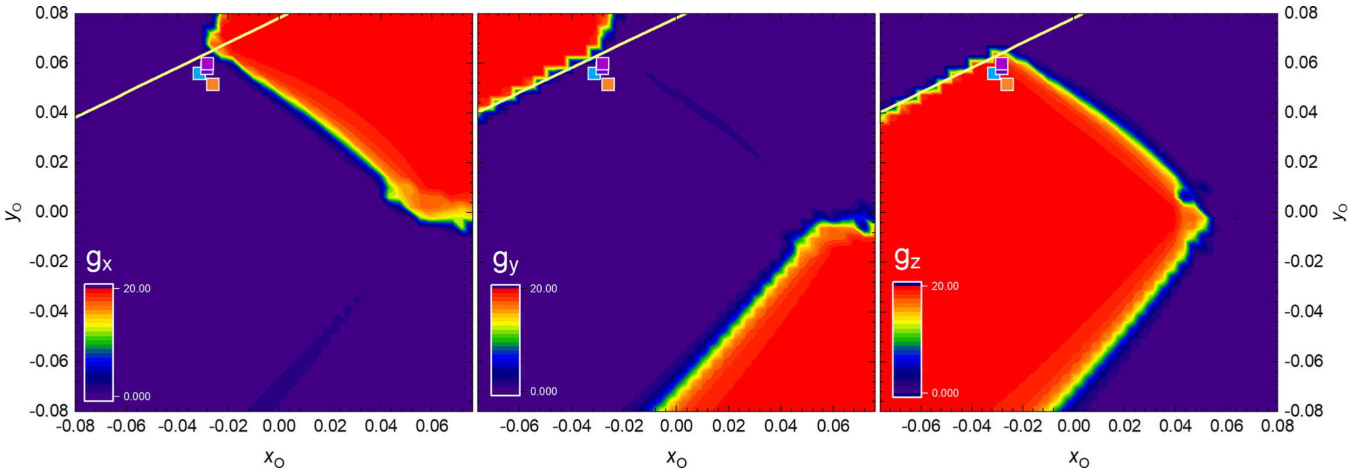

FIG. 6. Variations with the surrounding oxygen (x_O, y_O) coordinates of the Dy^{3+} Landé factors g_x, g_y, and g_z (respectively, left, middle, and right panels), calculated with a point-charge model (constant z_O). The colored squares show the experimental oxygen coordinates of the four synthesized garnets (Table I; color scheme identical to that of Figs. 3–5). The yellow line indicates the relationship $y_O = (x_O + z_O)/2$, which corresponds to the eight Dy-O distances all being equal in the dodecahedron. The (x_O, y_O) range is deliberately larger than what is achievable in dysprosium garnets for comprehensiveness.

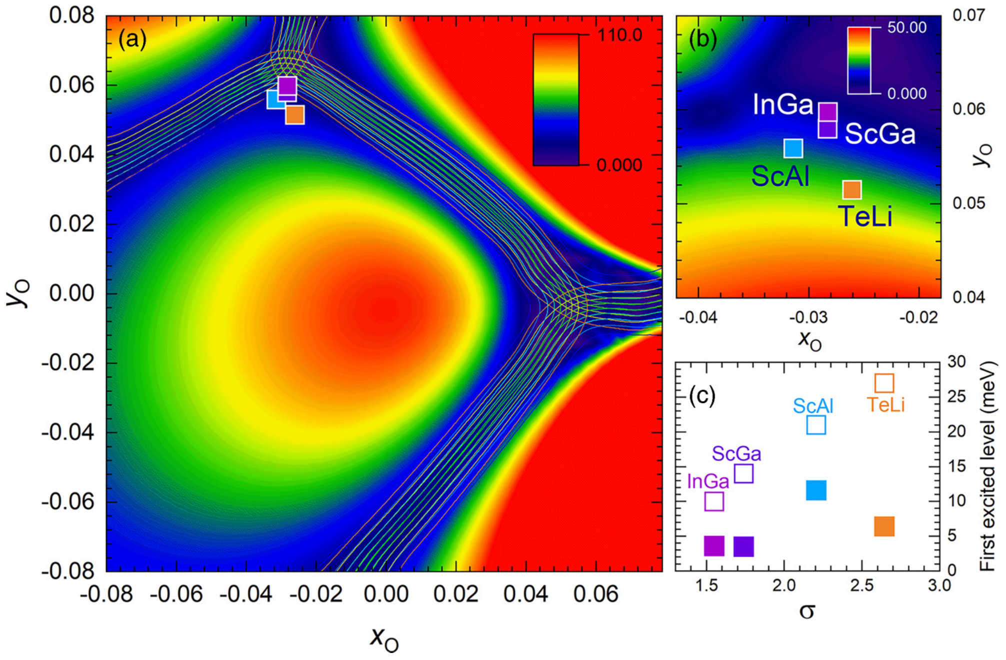

FIG. 7. (a) Variations with the surrounding oxygen (x_O, y_O) coordinates of the energy (in meV) of the first CEF excitation for a Dy^{3+} in its dodecahedron. The boundaries delimiting the different Ising phases are marked by contour lines. The (x_O, y_O) range is deliberately large for comprehensiveness. (b) Enlargement of (a) around the set of experimental data (as in Table I) displayed as colored squares. (c) Evolution with the variance σ of the calculated (empty squares) and experimental (full squares) energy of the first CEF excitation level for the different Dy garnets studied.

but which corresponds to an extremely distorted DyO$_8$ cage, involving unrealistic Dy-O distances (shorter than ~1.5 Å or larger than 3.5 Å). Figure 7 illustrates the dependence with (x_O, y_O) of the energy of the corresponding Dy^{3+} first crystal-field CEF excitation. As could be expected, the energy gap between the ground state and the first CEF excitation decreases as one gets nearer to an anisotropy boundary [pictured by contour lines, Fig. 7(a)], that is, as the Ising character is lost.

Although those calculations are only simple, as z_O is kept constant for instance, and only qualitative, they agree reasonably well with the experimental data, with DyScGa and DyInGa having lower energy first CEF excitations compared with DyTeLi or DyScAl [Figs. 7(b) and 7(c)], as observed experimentally. The discrepancy with DyTeLi, whose first excitation level is calculated to be larger than actually observed [Fig. 7(c)], certainly results from the fact that point-charge calculations are limited here to surrounding oxygen ions, not taking into account outer cationic shells and heterovalency effects. Although very simple, point charge modeling reproduces quite well, therefore both the Ising *Z* character of the Dy garnets studied here, and the fact that the closer to a regular cage, the closer to a *YZ* or *XZ* anisotropy.

In the calculations shown in Figs. 6 and 7, all the Wybourne coefficients authorized by the orthorhombic symmetry of the *R* site are taken into account. However, despite the complexity of the oxygen cage shape, whose precise impact on the Wybourne coefficients is difficult to apprehend, the existence of the three dominant Ising-*X*, -*Y*, or -*Z* regions can be easily understood, considering a simplified version of the electric potential distribution only, corresponding to a simpler analytical formula of $\mathcal{H}_{\rm CEF}$:

$$\mathcal{H}_{\rm CEF} = \frac{\alpha}{2}\left[3B_2^0 J_z^2 + \sqrt{6}B_2^2\left(J_x^2 - J_y^2\right)\right] = \frac{\alpha\sqrt{6}B_2^2}{2}\left[\frac{3B_2^0}{\sqrt{6}B_2^2}J_z^2 + \left(J_x^2 - J_y^2\right)\right] \qquad (1)$$

with J_x, J_y, and J_z the coordinates of the total kinetic moment in the local frame, respectively. α is a rare-earth dependent tabulated coefficient [40]. Since α is negative for Dy^{3+}, it is easy to deduce from (1) that, if $B_2^2 > 0$ and $\frac{3B_2^0}{\sqrt{6}B_2^2} < 1$, the anisotropy is Ising with local axis *X*; if $B_2^2 < 0$ and $\frac{3B_2^0}{\sqrt{6}|B_2^2|} < 1$, it is Ising with local axis *Y*, and Ising with local axis *Z* everywhere else. The variation of the ratio B_2^0/B_2^2 with (x_O, y_O) is illustrated in Fig. 8 together with the boundaries corresponding to $B_2^2 = 0$ (green dashed line) and $\frac{3B_2^0}{\sqrt{6}B_2^2} = 1$ (red dotted line). Examination of Fig. 8 shows that the reasoning presented above allows one to understand quite well the three regions determined from the Landé factor calculations shown in Fig. 6. This means that despite the complexity of the distortion of the dodecahedron around a Dy ion, it is the second-order moment of the electric potential that drives the anisotropy.

To go further, and in particular to better grasp how this information can be used in the design of more efficient magnetocaloric materials, the variation of magnetic entropy with temperature and for different applied magnetic fields (from 0 to 4 T) was calculated vs (x_O, y_O). To take into account the fact that the garnet structure hosts three different Dy^{3+} (still

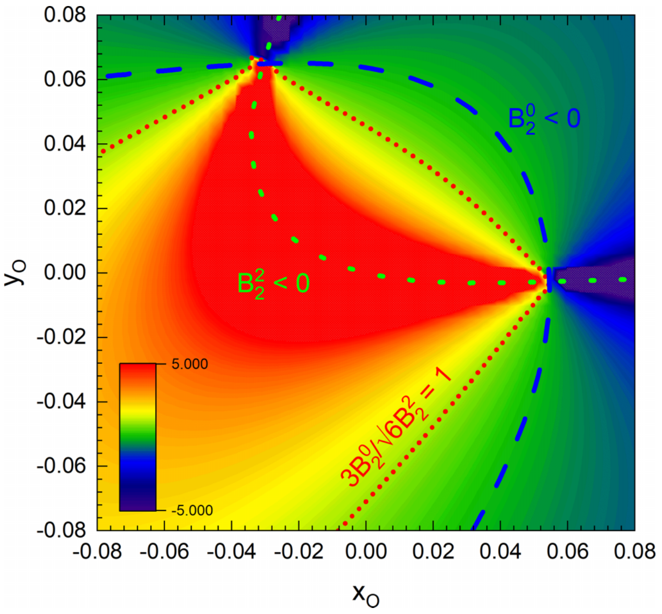

FIG. 8. Variation with the oxygen (x_O, y_O) coordinates in the garnet structure of the B_2^0/B_2^2 ratio characterizing the Dy^{3+} crystal field in its dodecahedral cage, calculated from a point-charge model (constant z_O). The green dashed line corresponds to the boundary $B_2^2 = 0$ and the red dotted line to the ratio $\frac{3B_2^0}{\sqrt{6}B_2^2} = 1$. The blue dashed line corresponds to $B_2^2 = 0$. The (x_O, y_O) range is deliberately large for comprehensiveness.

related by symmetry), with quantization axes either along the *a*, *b*, or *c* cubic axes, the calculations were carried out for a single Dy^{3+} with $Z = c$ quantization axis, but with the magnetic field applied along *X*, *Y*, and *Z*. Averaging the results, this approach was used to have an estimate of the magnetic entropy in a single crystal, without going into a more complex powder average calculation. From the resulting magnetic entropy curves $S_M(T, H)$ obtained, the magnetocaloric effect was extracted. Figures 9(a) and 9(b) show, for instance, the evolution with (x_O, y_O) of $-\Delta S_M(2\text{K})_{\Delta H=1\,\text{T}}$ and $-\Delta S_M(2\text{K})_{\Delta H=4\,\text{T}}$, respectively.

$-\Delta S_M(2\text{K})$ is strikingly uniform, more or less independent of x_O and y_O, except close to the transition lines between two types of anisotropy, where it is significantly larger. It gives a visual indication of the fact that close to boundaries, the magnetocaloric properties of Dy^{3+} are enhanced, as the Ising character of the latter weakens. Surprisingly, at the convergence between the three *X*, *Y*, and *Z* zones, this enhancement remains marginal, but at the moment it is unclear whether it is linked with a computational issue or not. To further illustrate this result, Figs. 9(c)–9(e) show $-\Delta S_M(T)$ calculated specifically for different and relevant (x_O, y_O) points located inside the Ising *Z* region [Fig. 9(c)], on the *XZ* line ([Fig. 9(d)] and close to the regular cage isotropic point [Fig. 9(e)]. At sufficiently low temperature, the Dy^{3+} ground state doublet is solely populated thus resulting in an effective spin 1/2, as mentioned earlier; hence, the magnetic entropy reservoir is narrowed to R ln(2) = 5.76 J K^{-1} mol^{-1} per Dy^{3+} at best. For most of the (x_O, y_O) pairs in Figs. 9(a) or 9(b), the magnetic anisotropy is of the Ising (-*X*, -*Y*, or -*Z*) type. This means, for magnetic fields remaining moderate, that only the magnetic moments whose anisotropy axis is parallel to the applied magnetic field will align. In other words, out of the three distinct Dy^{3+}, only one can release its entropy, hence $-\Delta S_M$ remains small: $-\Delta S_M(\text{max}) = -R\ln(2)/3$ at 2 K and $\Delta H = 1 - 4$ T. This behavior is illustrated in Fig. 9(c). In the planar (*XZ*) case [Fig. 9(d)], on the other hand, the magnetic entropy drops to zero for $H = 1$ T and above, for all three sites, leading to $-\Delta S_M(\text{max}) = R$ ln(2) below 1 K. Note that $-\Delta S_M$ is still substantial up to 5 K in 4 T in this case. For the most isotropic case [Fig. 9(e)], $-\Delta S_M$ drops quickly with temperature, so that even at 2 K, $\Delta H = 4$ T, $-\Delta S_M = 2.6$ J K^{-1} mol$_{\text{Dy}}^{-1}$.

IV. DISCUSSION

Point-charge modeling of a Dy^{3+} in an orthorhombic dodecahedral cage in which the oxygen (x_O, y_O) coordinates are varied leads to a "phase diagram" in which Ising-like anisotropies are predominant, either along the [001] axis of the cubic cell (Ising *Z*), along the [110] (Ising *X*), or the [1 − 10] (Ising *Y*) cell axis. Fitting this picture, DyAl has been known as an antiferromagnet with a strongly anisotropic Ising *Z* ($g_z \approx 18$, $g_x \approx g_y \leqslant 1$) ground state doublet for a long time [45–48]. With regard to the Dy garnets studied in the present work, DyScAl, DyTeLi, DyScGa, and DyInGa, the distortions of the DyO$_8$ cage determined by neutron diffraction also place them in the Ising *Z* zone, in agreement with inelastic neutron scattering experimental results. They are all, however, very close to the boundary between Ising *X*, *Y*, and *Z* anisotropies: this means that minute changes in O (x_O, y_O, z_O) can actually have a major impact on the magnetic behavior, despite seemingly very similar surroundings. Therefore, *B*/*C* site substitutions offer a potent way to achieve planar anisotropy.

The interest in achieving an *XZ* or *YZ* anisotropy is clear from the MCE values derived from magnetic entropy calculations performed in this work, however rudimentary they might be. A $-\Delta S_M(\text{max}) = R\ln(2) = 5.76$ J K^{-1} mol$_{\text{Dy}}^{-1}$ can be achieved close to this boundary below 2 K and even for a magnetic field change as low as $\Delta H \sim 1$ T (to be noted here is that MCE calculations are for single ions, and that long-range order will limit the range of temperature operation if $T_N > 2$ K), motivating future use in adiabatic demagnetization refrigeration systems. It is somewhat tricky to compare directly this calculation with MCE literature values, which have been obtained in specific experimental conditions, but to give a few examples, Mukherjee *et al.* reported on powder samples values of $-\Delta S_M(2\text{K})_{\Delta H=2\,\text{T}} = 3.09$ J K^{-1} mol$_{\text{Dy}}^{-1}$ for DyScAl, up to $-\Delta S_M(2\text{K})_{\Delta H=2\,\text{T}} = 3.77$ J K^{-1} mol$_{\text{Dy}}^{-1}$ for DyGa [29]. An enhanced magnetocaloric effect was also observed in Dy$_3$CrGa$_4$O$_{12}$, where it reached $-\Delta S_M(2\text{K})_{\Delta H=2\,\text{T}} = 4.50$ J K^{-1} mol$_{\text{Dy}}^{-1}$ [49]. On the other hand, recent measurements on a single crystal of DyGa, with the field applied along [110], led to $-\Delta S_M(2\text{K})_{\Delta H=2\,\text{T}} = 4.97$ J K^{-1} mol$_{\text{Dy}}^{-1}$, that is, very close to the theoretical maximum.

Coupled with MCE calculations, the phase diagram of the magnetic anisotropy in Dy garnets is a very powerful tool, which should be extended to investigate the properties of other rare earths, changing the *α*, *β*, and *γ* coefficients and the radial integrals specific to each rare earth. In this work, it also gives a clear clue as to why DyGa exhibits

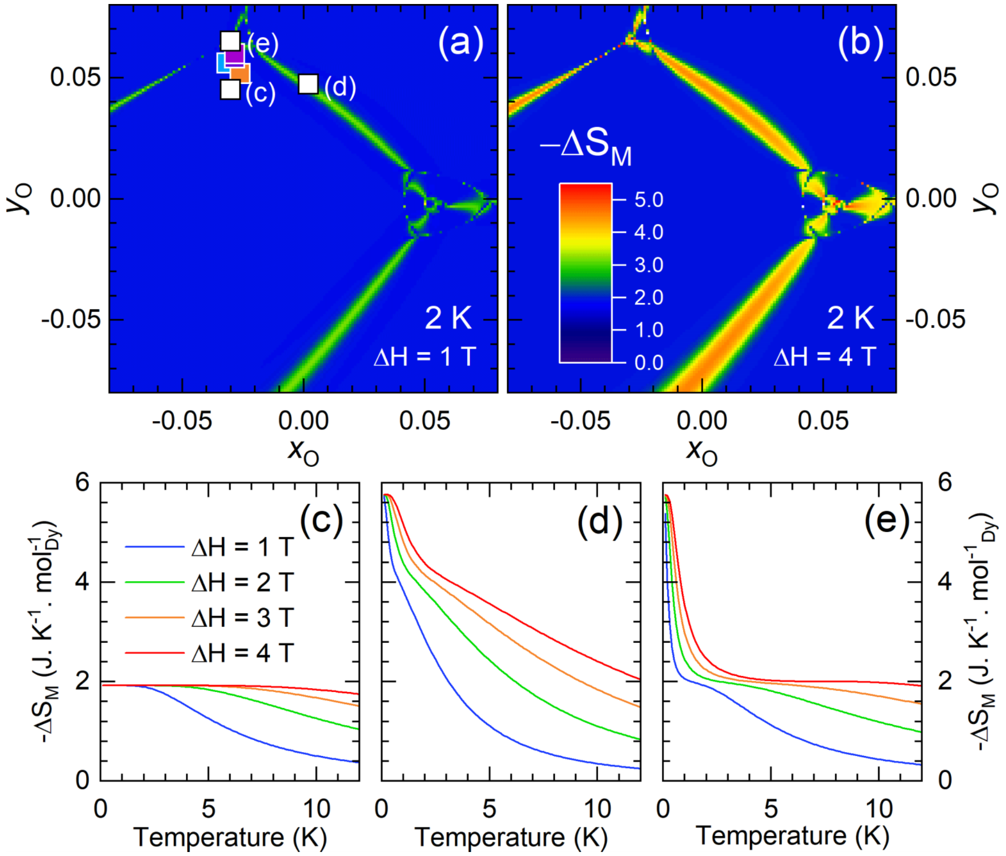

FIG. 9. (a) and (b) illustrate the variation of $-\Delta S_M(2\text{K})_{\Delta H=1\text{T}}$ and $-\Delta S_M(2\text{K})_{\Delta H=4\text{T}}$ with $(x_\text{O},\ y_\text{O})$ (in J K^{-1} mol$_{\text{Dy}}^{-1}$). The color scale is the same in both (a) and (b). The colored square symbols correspond to the $(x_\text{O},\ y_\text{O})$ coordinates of the garnets synthesized for this work. (c)–(e) show the theoretical magnetic entropy variation $-\Delta S_M$, calculated from the magnetic entropy curves vs temperature and magnetic field for three interesting $(x_\text{O},\ y_\text{O})$ points (−0.03,0.045) (c), (0.002,0.047) (d), and (−0.03,0.065) (e) (white square symbols). The $(x_\text{O},\ y_\text{O})$ range is deliberately large for comprehensiveness.

the best magnetocaloric properties in this family so far. It is the only known dysprosium garnet with clear *XZ* magnetic anisotropy [20], having puzzled scientists for several decades beforehand [50–54]. Unfortunately there is no structural data available on this compound that is accurate enough to place it reliably on the phase diagram. It is reasonable, however, to state that, being close to the *XZ* boundary, the distortion of the DyO$_8$ cage is probably smaller than in all other garnets studied, which would be in agreement with the conclusions of Kibalin *et al.* [20].

The main challenge now remains to investigate the effect of the *B* and *C* sites cationic size and mismatch on the rare-earth oxygen environment. This is not a straightforward matter as the dodecahedral cage in garnets is quite robust against distortions, as those also involve distortions of neighboring and rather rigid tetrahedral and octahedral cages.

Very schematically, less chemical pressure (large cell parameters) favors a more regular dodecahedron, and hence a weaker Ising character: all the compounds with the large Ga cation on the *C* site have lower energy crystal-field levels; nevertheless, a large cation on the *C* site is not sufficient to induce this, nor is a large cell, since DyInGa still exhibits an Ising anisotropy when DyGa does not. Considerations on oxygen distances in the cage do not indicate any reliable trend either. The magnetic anisotropy phase diagram points out the pertinence of a structural boundary on which all Dy-O distances are equal, but it is not evident how to achieve such a regular environment from the comparison of four compositions only; in particular, accurate structural data on the oxygen position in DyGa are mandatory to confirm whether the latter is close to this structural boundary or not.

It is also clear in this work that calculations point out interesting areas outside the range of $(x_\text{O},\ y_\text{O})$ positions reachable in dysprosium garnet oxides. A possibility to explore those areas would be to find other, lesser packed, rare-earth systems with a D_2 symmetry site for the rare earth; neutron diffraction experiments under pressure could be an interesting way as well to study *in situ* magnetic anisotropy changes as the cage distorts. One other possible route is the synthesis of nonoxide garnets [55], like oxisulfides, which, although very promising, are outside the scope of the present paper.

DyGa still remains an anomaly amongst dysprosium garnet oxides. If a large *C* site cation and a small *B* site cation are necessary to achieve a regular Dy cage, it should prove challenging to synthesize, especially with *B*-*C* intersite substitutions being already present. Disorder of that type actually might be worth investigating further, as it might blur the boundaries between Ising zones. Besides better MCE properties, the quest for an *XZ* garnet also remains appealing because of the competition between dipolar interactions and magnetic exchange that it allows, which is thought to be responsible for the very low T_N in DyGa [56], and which on a hyperkagome lattice, should lead to interesting exotic ground states.

V. CONCLUSION

Investigations of the structural and magnetic properties of the four dysprosium garnets $Dy_3Sc_2Al_3O_{12}$, $Dy_3Te_2Li_3O_{12}$, $Dy_3Sc_2Ga_3O_{12}$, and $Dy_3In_2Ga_3O_{12}$, were carried out to understand the evolution, with substitutions on the B and C sites, of the Dy^{3+} magnetic anisotropy and its relationship with the distortion of its oxygen environment. From point-charge calculations, we were able to infer that the shape of the DyO_8 cage in the garnets studied places Dy^{3+} in the strong Ising Z ground state, although very close to the X-Z and Y-Z boundaries. The closer to an anisotropy boundary, the more pronounced the planar anisotropy character, and the larger the magnetic entropy drop at low temperature and low field, confirming the potential of Dy garnets for adiabatic demagnetization refrigeration devices. Easily extendable to other rare earths and to different crystal structures, CEF calculations of this type should prove useful to anticipate and improve the magnetocaloric properties of rare-earth materials.

ACKNOWLEDGMENTS

This work was partially supported by the ANR funding SAKE (ANR-22-CE50-0023-01). Part of this work is based on experiments performed at the Swiss spallation neutron source SINQ, Paul Scherrer Institute, Villigen, Switzerland. These experiments were financially supported by the Fédération Française de la Neutronique (2FDN).

APPENDIX

Crystal electric field calculations have been first carried out using the complete description of the $4f$ shell of the Dy^{3+} ion. Having nine electrons to distribute over the 14 available states, the dimension of the Hilbert basis is 2002. In Dy^{3+}, the ground state multiplet has $J = 15/2$ (spanned by 16 basis vectors) and is very well separated from the first excited multiplet, located at around 430 meV, thanks to a large spin orbit coupling 237.2 meV [57]. This property allows one to use instead the Stevens formalism, hence working directly in the ground multiplet, and consider the Stevens Hamiltonian: $H = \sum_{l,m} b_{l,m}\, O_{l,m}$. The O_{lm} and b_{lm} are, respectively, the equivalent Stevens operators and Stevens coefficients, determined from the Wybourne B_{lm} coefficients as: $b_{lm} = \mu_J\ \theta_{l,m}\ B_{l,m}$. In the case of Dy^{3+}, $\mu_J = \alpha_J = \frac{-2,}{5\times7\times9}$, $\beta_J = \frac{-8}{27\times5\times7\times11\times13}$, $\gamma_J = \frac{4}{27\times7\times121\times169}$ for $l = 2,\ 4,\ 6$. The $\theta_{l,m}$ are given in the table below:

l, m	$m = 0$	$m = 1$	$m = 2$	$m = 3$	$m = 4$	$m = 5$	$m = 6$
$l = 2$	$1/2$	$\sqrt{6}$	$\sqrt{6}/2$				
$l = 4$	$1/8$	$\sqrt{5}/2$	$\sqrt{10}/4$	$\sqrt{35}/2$	$\sqrt{70}/8$		
$l = 6$	$1/16$	$\sqrt{42}/8$	$\sqrt{105}/16$	$\sqrt{105}/8$	$3\sqrt{14}/6$	$3\sqrt{77}/8$	$\sqrt{231}/16$

The Wybourne coefficients entering the CEF Hamiltonian are estimated using the point-charge model:

$$B_{l,m} = \sum_k Z_k \frac{a_0^l\, R_l}{d_k^{l+1}}\,(-1)^m \sqrt{\frac{4\pi}{2l+1}}\, Y_{l,m}(\theta_k,\ \varphi_k),$$

where a_0 is the Bohr radius, $Y_{l,m}$ is the (l, m) spherical harmonic, the R_l are radial integrals which depend on the rare-earth ion $R_l = 0.78,\ 1.505,\ 6.048$ for $l = 2,\ 4,\ 6$, $(\vartheta_k,\ \varphi_k,\ d_k)$ are the spherical coordinates of neighboring atoms labeled k, and Z_k is their charge. For the sake of simplicity, we consider the Dy ion at $R_O = (\frac{2}{16}, 0, \frac{3}{12})$ as well as its O cage, limited to nearest neighbors, with atomic positions R_k :

$$(1/4 - x, 1/4 - z, 1/4 - y),\quad (1/4 - z, 1/4 - y, 1/4 - x),\quad (1/4 - x, -1/4 + z, 1/4 + y),$$
$$(1/4 - z, -1/4 + y, 1/4 + x),\quad (x, -y, 1/2 - z),\quad (z, -x, 1/2 - y),\quad (x, y, z),\quad (z, x, y)$$

We then transform those cubic coordinates as $R'_k = \begin{pmatrix} 0 & 1/\sqrt{2} & -1/\sqrt{2} \\ 0 & 1/\sqrt{2} & 1/\sqrt{2} \\ 1 & 0 & 0 \end{pmatrix} [R_k - R_O]$ to use the X, Y, Z frame defined in the text. Diagonalization of H gives the eigenvectors $|n\rangle$, and eigenvalues $|E_n\rangle$, from which are inferred the partition function $Z = \mathrm{Tr}[e^{-H/T}] = \sum_n e^{-E_n/T}$, the free energy $F = -\ln Z$, and finally the entropy

$$S = \frac{E}{T} + \ln Z = \frac{\frac{1}{Z}\sum_n E_n\, e^{-E_n/T}}{T} + \ln Z.$$

[1] T. Numazawa, K. Kamiya, T. Utaki, and K. Matsumoto, Magnetic refrigerator for hydrogen liquefaction, Cryogenics **62**, 185 (2014).

[2] V. Franco, J. Blázquez, J. Ipus, J. Law, L. Moreno-Ramírez, and A. Conde, Magnetocaloric effect: From materials research to refrigeration devices, Prog. Mater. Sci. **93**, 112 (2018).

[3] P. Baptista de Castro, K. Terashima, T. D. Yamamoto, Z. Hou, S. Iwasaki, R. Matsumoto, S. Adachi, Y. Saito, P. Song, H. Takeya, and Y. Takano, Machine-learning-guided discovery of the gigantic magnetocaloric effect in HoB_2 near the hydrogen liquefaction temperature, NPG Asia Mater. **12**, 35 (2020).

[4] X. Tang, H. Sepehri-Amin, N. Terada, A. Martin-Cid, I. Kurniawan, S. Kobayashi, Y. Kotani, H. Takeya, J. Lai, Y. Matsushita, T. Ohkubo, Y. Miura, T. Nakamura, and K. Hono, Magnetic refrigeration material operating at a full temperature range required for hydrogen liquefaction, Nat. Commun. **13**, 1817 (2022).

[5] M. Evangelisti, O. Roubeau, E. Palacios, A. Camon, T. N. Hooper, E. K. Brechin, and J. J. Alonso, Cryogenic magnetocaloric effect in a ferromagnetic molecular dimer, Angew. Chem., Int. Ed. **50**, 6606 (2011).

[6] D. Jang, T. Gruner, A. Steppke, K. Mitsumoto, C. Geibel, and M. Brando, Large magnetocaloric effect and adiabatic demagnetization refrigeration with $YbPt_2Sn$, Nat. Commun. **6**, 8680 (2015).

[7] M. E. Zhitomirsky, Enhanced magnetocaloric effect in frustrated magnets, Phys. Rev. B **67**, 104421 (2003).

[8] M. Kleinhans, K. Eibensteiner, J. Leiner, C. Resch, L. Worch, M. Wilde, J. Spallek, A. Regnat, and C. Pfleiderer, Magnetocaloric properties of $R_3Ga_5O_{12}$ (R = Tb, Gd, Nd, Dy), Phys. Rev. Appl. **19**, 014038 (2023).

[9] D. A. Paixao Brasiliano, J.-M. Duval, C. Marin, E. Bichaud, J.-P. Brison, M. Zhitomirsky, and N. Luchier, YbGG material for adiabatic demagnetization in the 100 mK–3 K range, Cryogenics **105**, 103002 (2020).

[10] A. Rousseau, J.-M. Parent, and J. A. Quilliam, Anisotropic phase diagram and spin fluctuations of the hyperkagome magnet $Gd_3Ga_5O_{12}$ as revealed by sound velocity measurements, Phys. Rev. B **96**, 060411(R) (2017).

[11] E. Lhotel, L. Mangin-Thro, E. Ressouche, P. Steffens, E. Bichaud, G. Knebel, J.-P. Brison, C. Marin, S. Raymond, and M. E. Zhitomirsky, Spin dynamics of the quantum dipolar magnet $Yb_3Ga_5O_{12}$ in an external field, Phys. Rev. B **104**, 024427 (2021).

[12] J. A. M. Paddison, H. Jacobsen, O. A. Petrenko, M. T. Fernandez-Diaz, P. P. Deen, and A. L. Goodwin, Hidden order in spin-liquid $Gd_3Ga_5O_{12}$, Science **350**, 179 (2015).

[13] P. P. Deen, O. Florea, E. Lhotel, and H. Jacobsen, Updating the phase diagram of the archetypal frustrated magnet $Gd_3Ga_5O_{12}$, Phys. Rev. B **91**, 014419 (2015).

[14] L. Ø. Sandberg, R. Edberg, I.-M. B. Bakke, K. S. Pedersen, M. C. Hatnean, G. Balakrishnan, L. Mangin-Thro, A. Wildes, B. Fåk, G. Ehlers, G. Sala, P. Henelius, K. Lefmann, and P. P. Deen, Emergent magnetic behavior in the frustrated $Yb_3Ga_5O_{12}$ garnet, Phys. Rev. B **104**, 064425 (2021).

[15] J. Khatua, S. Bhattacharya, Q. P. Ding, S. Vrtnik, A. M. Strydom, N. P. Butch, H. Luetkens, E. Kermarrec, M. S. R. Rao, A. Zorko, Y. Furukawa, and P. Khuntia, Spin liquid state in a rare-earth hyperkagome lattice, Phys. Rev. B **106**, 104404 (2022).

[16] R. Wawrzynczak, B. Tomasello, P. Manuel, D. Khalyavin, M. D. Le, T. Guidi, A. Cervellino, T. Ziman, M. Boehm, G. J. Nilsen, and T. Fennell, Magnetic order and single-ion anisotropy in $Tb_3Ga_5O_{12}$, Phys. Rev. B **100**, 094442 (2019).

[17] U. Loew, S. Zherlitsyn, K. Araki, M. Akatsu, Y. Nemoto, T. Goto, U. Zeitler, and B. Luethi, Magneto-elastic effects in $Tb_3Ga_5O_{12}$, J. Phys. Soc. Jpn. **83**, 044603 (2014).

[18] S. Petit, F. Damay, Q. Berrod, and J. M. Zanotti, Spin and lattice dynamics in the two-singlet system $Tb_3Ga_5O_{12}$, Phys. Rev. Res. **3**, 013030 (2021).

[19] Y. Cai, M. N. Wilson, J. Beare, C. Lygouras, G. Thomas, D. R. Yahne, K. Ross, K. M. Taddei, G. Sala, H. A. Dabkowska, A. A. Aczel, and G. M. Luke, Crystal fields and magnetic structure of the Ising antiferromagnet $Er_3Ga_5O_{12}$, Phys. Rev. B **100**, 184415 (2019).

[20] I. Kibalin, F. Damay, X. Fabrèges, A. Gukasov, and S. Petit, Magnetic anisotropy of dysprosium garnets, Phys. Rev. Res. **2**, 033509 (2020).

[21] N. Terada, H. Mamiya, H. Saito, T. Nakajima, T. D. Yamamoto, K. Terashima, H. Takeya, O. Sakai, S. Itoh, Y. Takano, M. Hase, and H. Kitazawa, Crystal electric field level scheme leading to giant magnetocaloric effect for hydrogen liquefaction, Commun. Mater. **4**, 13 (2023).

[22] F. Damay and E. Suard, Crystal structure of rare-earth $Dy_3B_2C_3O_{12}$ garnets, Institut Laue-Langevin (ILL) (2021), doi: 10.5291/ILL-DATA.EASY-857.

[23] F. Damay, C. Colin, and S. Petit, Magnetic ground states of rare-earth $Dy_3B_2C_3O_{12}$, Institut Laue-Langevin (ILL) (2021), doi: 10.5291/ILL-DATA.CRG-2780.

[24] J. Rodriguez-Carvajal, Recent advances in magnetic-structure determination by neutron powder diffraction, Phys. B (Amsterdam, Neth.) **192**, 55 (1993).

[25] E. Kroumova, M. I. Aroyo, J. M. Perez-Mato, A. Kirov, C. Capillas, S. Ivantchev, and H. Wondratschek, Bilbao crystallographic server: Useful databases and tools for phase-transition studies, Phase Transitions **76**, 155 (2003).

[26] M. I. Aroyo, A. Kirov, C. Capillas, J. M. Perez-Mato, and H. Wondratschek, Bilbao crystallographic server. II. Representations of crystallographic point groups and space groups, Acta Crystallogr. Sect. A: Found. Adv. **62**, 115 (2006).

[27] F. Damay, C. Decorse, E. Lhotel, S. Petit, and S. Rols, Evolution of the Dy^{3+} magnetic anisotropy in $Dy_3B_2C_3O_{12}$ garnets, Institut Laue-Langevin (ILL) (2021), doi:10.5291/ILL-DATA.4-04-505.

[28] J. Mesot, S. Janssen, L. Holitzner, and R. Hempelmann, Focus: Project of a space and time focussing time-of-flight spectrometer for cold neutrons at the Spallation Source SINQ of the Paul Scherrer Institute, J. Neutron Res. **3**, 293 (1996).

[29] P. Mukherjee, A. C. S. Hamilton, H. F. J. Glass, and S. E. Dutton, Sensitivity of magnetic properties to chemical pressure in lanthanide garnets $Ln_3A_2X_3O_{12}$, Ln = Gd, Tb, Dy, Ho, A = Ga, Sc, In, Te, X = Ga, Al, Li, J. Phys.: Condens. Matter **29**, 405808 (2017).

[30] M. P. O'Callaghan, D. R. Lynham, E. J. Cussen, and G. Z. Chen, Structure and ionic-transport properties of lithium-containing garnets $Li_3Ln_3Te_2O_{12}$ (Ln = Y, Pr, Nd, Sm-Lu), Chem. Mater. **18**, 4681 (2006).

[31] F. A. Cevallos, S. Guo, and R. J. Cava, Magnetic properties of lithium-containing rare earth garnets $Li_3RE_3Te_2O_{12}$ (RE = Y, Pr, Nd, Sm-Lu), Mater. Res. Express **5**, 126106 (2018).

[32] R. D. Shannon, Revised effective ionic-radii and systematic studies of interatomic distances in halides and chalcogenides, Acta Crystallogr. Sect. A: Found. Adv. **32**, 751 (1976).

[33] F. Euler and J. Bruce, Oxygen coordinates of compounds with garnet structure, Acta Crystallogr. **19**, 971 (1965).

[34] H. W. Capel, Magnetic properties of rare earth ions in aluminium and gallium garnets, Physica **31**, 1152 (1965).

[35] S. J. Gomez, P. M. Sarte, M. Zelensky, A. M. Hallas, B. A. Gonzalez, K. H. Hong, E. J. Pace, S. Calder, M. B. Stone, Y. Su, E. Feng, M. D. Le, C. Stock, J. P. Attfield, S. D. Wilson, C. R. Wiebe, and A. A. Aczel, Absence of moment fragmentation in the mixed B-site pyrochlore Nd_2GaSbO_7, Phys. Rev. B **103**, 214419 (2021).

[36] P. M. Sarte, K. Cruz-Kan, B. R. Ortiz, K. H. Hong, M. M. Bordelon, D. Reig-i Plessis, M. Lee, E. S. Choi, M. B. Stone, S. Calder, D. M. Pajerowski, L. Mangin-Thro, Y. Qiu, J. P. Attfield, S. D. Wilson, C. Stock, H. D. Zhou, A. M. Hallas, J. A. M. Paddison, A. A. Aczel, and C. R. Wiebe, Dynamical ground state in the XY pyrochlore Yb_2GaSbO_7, npj Quantum Mater. **6**, 42 (2021).

[37] C. Mauws, N. Hiebert, M. L. Rutherford, H. D. Zhou, Q. Huang, M. B. Stone, N. P. Butch, Y. Su, E. S. Choi, Z. Yamani, and C. R. Wiebe, Magnetic ordering in the Ising antiferromagnetic pyrochlore Nd_2ScNbO_7, J. Phys.: Condens. Matter **33**, 245802 (2021).

[38] A. Scheie, M. Sanders, X. Gui, Y. Qiu, T. R. Prisk, R. J. Cava, and C. Broholm, Beyond magnons in Nd_2ScNbO_7: An Ising pyrochlore antiferromagnet with all-in-all-out order and random fields, Phys. Rev. B **104**, 134418 (2021).

[39] B. D. Gaulin, E. Kermarrec, M. L. Dahlberg, M. J. Matthews, F. Bert, J. Zhang, P. Mendels, K. Fritsch, G. E. Granroth, P. Jiramongkolchai, A. Amato, C. Baines, R. J. Cava, and P. Schiffer, Quenched crystal-field disorder and magnetic liquid ground states in $Tb_2Sn_{2-x}Ti_xO_7$, Phys. Rev. B **91**, 245141 (2015).

[40] M. T. Hutchings, Point-charge calculations of energy levels of magnetic ions in crystalline electric fields, Solid State Phys. **16**, 227 (1964).

[41] R. M. Sternheimer, M. Blume, and R. F. Peierls, Shielding of crystal fields at rare-earth ions, Phys. Rev. **173**, 376 (1968).

[42] Z. Dun, X. Bai, M. B. Stone, H. Zhou, and M. Mourigal, Effective point-charge analysis of crystal fields: Application to rare-earth pyrochlores and tripod kagome magnets $R_3Mg_2Sb_3O_{14}$, Phys. Rev. Res. **3**, 023012 (2021).

[43] Z. Zolnierek, Crystal field parameters in a modified point charge model, J. Phys. Chem. Solids **45**, 523 (1984).

[44] M. T. Hutchings and D. K. Ray, Investigation into origin of crystalline electric field effects on rare earth ions: I. Contribution from neighbouring induced moments, Proc. Phys. Soc. London **81**, 663 (1963).

[45] M. Ball, W. P. Wolf, M. J. M. Leask, and A. F. G. Wyatt, Thermal properties of dysprosium aluminum garnet near Néel temperature, J. Appl. Phys. **34**, 1104 (1963).

[46] M. Ball, W. P. Wolf, and A. F. G. Wyatt, Magnetic transitions in dysprosium aluminum garnet, J. Appl. Phys. **35**, 937 (1964).

[47] J. M. Hastings, L. M. Corliss, and C. G. Windsor, Antiferromagnetic structure of dysprosium aluminum garnet, Phys. Rev. **138**, A176 (1965).

[48] J. C. Norvell, W. P. Wolf, L. M. Corliss, J. M. Hastings, and R. Nathans, Magnetic neutron scattering in dysprosium aluminum garnet. I. Long-range order, Phys. Rev. **186**, 557 (1969).

[49] P. Mukherjee and S. E. Dutton, Enhanced magnetocaloric effect from Cr substitution in Ising lanthanide gallium garnets $Ln_3CrGa_4O_{12}$ ($Ln =$ Tb, Dy, Ho), Adv. Funct. Mater. **27**, 1701950 (2017).

[50] W. Wolf, M. Ball, M. Hutchings, M. Leask, M. J. H, and A. Wyatt, The magnetic properties of rare earth ions in garnets, J. Phys. Soc. Jpn. **17 Supp. B-1**, 443 (1962).

[51] M. Veyssie and B. Dreyfus, Champ cristallin au niveau de l'ion terre rare dans les gallates de dysprosium et de samarium a structure grenat, J. Phys. Chem. Solids **28**, 499 (1967).

[52] J. Blanc, D. Brochier, and A. Ribeyron, Study of the fundamental multiplet of Dy^{3+} in DyGaG and DyAlG, Phys. Lett. A **33**, 201 (1970).

[53] R. L. Wadsack, J. L. Lewis, B. E. Argyle, and R. K. Chang, Phonons and crystal field levels in dysprosium garnets by Raman scattering, Phys. Rev. B **3**, 4342 (1971).

[54] J. Filippi, F. Tcheou, and J. Rossat-Mignod, Crystal-field effect on the paramagnetic properties of Dy^{3+} ion in dysprosium gallium garnet, Solid State Commun. **33**, 827 (1980).

[55] J. Schmidt, H.-C. Wang, G. Schmidt, and M. A. L. Marques, Machine learning guided high-throughput search of non-oxide garnets, npj Comput. Mater. **9**, 63 (2023).

[56] J. Filippi, J. C. Lasjaunias, A. Ravex, F. Tcheou, and J. Rossat-Mignod, Specific-heat of dysprosium gallium garnet between 37 mK and 2 K, Solid State Commun. **23**, 613 (1977).

[57] A. J. Freeman and J. P. Desclaux, Dirac-Fock studies of some electronic properties of rare-earth ions, J. Magn. Magn. Mater. **12**, 11 (1979).